Numerical investigation of ion-energy-distribution functions in single and dual frequency capacitively coupled plasma reactors

V. Georgieva,* A. Bogaerts, and R. Gijbels

Department of Chemistry, University of Antwerp, Universiteitsplein 1, B-2610 Wilrijk-Antwerp, Belgium

(Received 8 September 2003; revised manuscript received 5 December 2003; published 23 February 2004)

Ion-energy-distribution functions (IEDFs) are numerically investigated in capacitively coupled (cc) radio frequency (rf) $Ar/CF_4/N_2$ discharges by a one-dimensional particle-in-cell/Monte Carlo model. The simulation considers electron-neutral collisions, various kinds of collisions of ions (Ar^+, CF_3^+, N_2^+, F^-, and CF_3^-) with neutral, positive-negative ion, and electron-ion recombination. The influence of pressure, applied voltage amplitude, and applied frequency on the Ar^+, CF_3^+, and N_2^+ IEDFs is presented. The dependence on the frequency regime is investigated by simulations of the $Ar/CF_4/N_2$ mixture in single (13.56 MHz) and dual frequency ($2+27$ MHz or $1+27$ MHz) cc reactors. A comparison of the simulation results with analytical calculations in a collisionless rf sheath is discussed. The results show that the IEDFs shift toward the low energies with increasing pressure or decreasing applied voltage amplitude. The Ar^+ and N_2^+ IEDFs exhibit secondary maxima due to the charge transfer collisions. The CF_3^+ IEDF has a peak at high energies in consistency with the average sheath potential drop. The IEDFs in the dual frequency regime are broad and bimodal.

I. INTRODUCTION

In plasma etching the kinetics of the ions incident on the wafer is crucial in determining the etch rates and anisotropy. This explains the extensive experimental [1–8], analytical [9–11], and numerical [2,3,10,12–16] studies of the ion-energy-distribution function (IEDF) in capacitively coupled (cc) radio frequency (rf) reactors. A good review and analysis of theoretical and experimental investigations of the IEDF are given by Kawamura *et al.* [10]. The main points can be summarized as follows.

(a) In collisionless sheaths the crucial parameter determining the shape of the IEDF is the relation τ_{ion}/τ_{rf}, where τ_{ion} is the ion transit time and $\tau_{rf}=2\pi/\omega_{rf}$ is the rf period. The ion transit time is calculated by [10]

$$\tau_{ion}=3\bar{s}\left(\frac{M}{2e\bar{V}_s}\right)^{1/2},\qquad(1)$$

where $\bar{s}$ is the time-averaged sheath thickness, $\bar{V}_s$ is the average sheath potential drop, M is the ion mass, and e is the electron charge.

If $\tau_{ion}/\tau_{rf}\gg1$, i.e., at high frequency (HF), the ions respond to the average sheath potential drop resulting in a narrow IEDF with one or two maxima depending on the value of τ_{ion}/τ_{rf}. If $\tau_{ion}/\tau_{rf}\ll1$, i.e., at low frequency (LF), the ions respond to the instantaneous sheath potential drop resulting in a broad and bimodal IEDF.

(b) In collisional sheaths charge exchange collisions lead to the appearance of secondary maxima at energies lower than the primary maxima, and both charge exchange and elastic collisions shift the IEDF to lower energies.

The sheaths in conventional rf etching reactors are typically collisional. Analytical models assume limiting approximations such as constant sheath width, sinusoidal sheath potential drop, etc., and therefore give only the qualitative features of the IEDF. Experimental measurements as well as numerical methods present more reliable results. Particle-in-cell (PIC) simulations of rf discharges are attractive for calculation of the particle energy distributions since the distributions can be obtained self-consistently from first principle [17]. Collisional effects are included by coupling the PIC model with a Monte Carlo (MC) collision method [18–20].

Most of the experimental and numerical papers deal with an Ar plasma because of its simple chemistry [1–3,5–7,13,16]. Feed-gas mixes are usually complex because of the conflicting requirements on the etch rate, selectivity to mask, and anisotropy. Carbon tetrafluoride CF_4 is a basic component in gas mixtures for plasma etching of silicon and silicon dioxide [21]. The purpose of the present work is a detailed numerical investigation of Ar^+, CF_3^+, and N_2^+ IEDFs in cc rf $Ar/CF_4/N_2$ discharges at a range of different pressures, applied voltages, and frequencies, by means of a one-dimensional PIC/MC method.

In our first paper we presented a one-dimensional PIC/MC model and clarified the plasma structure and parameters in Ar, CF_4, and Ar/CF_4 discharges [22]. In the next paper the model was extended to examine the discharge structure in a mixture of Ar, CF_4 and N_2, which is a feedstock gas for etching in industrial cc dual-frequency reactors [23]. Simulations were performed for a 0.8/0.1/0.1 ratio of $Ar/CF_4/N_2$ mixture at a pressure of 30 mTorr in single (13.56 MHz) and dual ($2+27$ MHz) frequency cc reactors and a comparison between the two frequency regimes was made. The calculated IEDFs were presented along with other results of the model, i.e., potential and electric field distributions, particle densities, and electron energy distribution function. The results show that the LF-HF scheme provides a

*Electronic address: Violeta.Georgieva@ua.ac.be
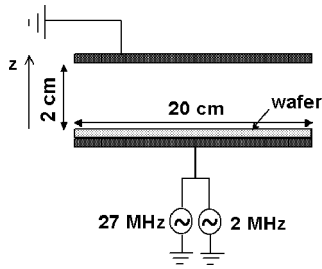
FIG. 1. Schematic diagram of the dual frequency reactor.

significantly wider ion bombardment energy range in comparison with the single HF configuration. Although several other works investigated plasma properties in dual frequency reactors by experimental measurements or numerical simulations [e.g., Refs. [16], [24–30]] detailed studies of the ion bombardment energy are very scarce. For example, only the average ion bombardment energy is given in Refs. [24–26]. Myers *et al.* predicted ion energies and angular distributions in single and dual frequency regimes by combining a single and dual frequency plasma sheath model with a Monte Carlo simulation of ion transport [16].

In the present paper the simulations are carried out over a wide range of pressure, applied voltage, and frequency. One group of calculations is performed for an applied voltage amplitude of 300 V at pressures of 20, 30, 50, 70, 100, and 200 mTorr. Another group of simulations is carried out for applied voltage amplitudes of 200, 300, 500 and 700 V at a pressure of 30 mTorr. Both groups consider a conventional cc rf (13.56 MHz) reactor. The dependence on the frequency regime is investigated by simulations of the $Ar/CF_4/N_2$ mixture at a pressure of 30 mTorr in single (13.56 MHz) and dual frequency (2+27 MHz or 1+27 MHz) cc reactors. An analytical model of the IEDF in a collisionless rf sheath in a dual frequency reactor is developed and a comparison of the simulation results with the analytical results is discussed. The time evolution of the IEDF during the rf cycle is also presented.

In Sec. II the input parameters, the outline of the numerical and analytical models, and the collisions included in the simulation are given. In Sec. III the results of the simulations for Ar^+, CF_3^+, and N_2^+ IEDFs are presented and discussed. Finally, in Sec. IV a summary is given. All cross section data of the ion-neutral collisions used in the model are presented in the Appendix.

II. DESCRIPTION OF THE MODELS

A. PIC/MC model

Two types of reactors are considered in this study. One type is the conventional cc rf (13.56 MHz) reactor. The other type is a cc dual frequency (LF-HF) reactor and its schematic diagram is shown in Fig. 1. The plasma is sustained between two parallel plates, each 20 cm in diameter and separated from the other by 2 cm. One of the electrodes is driven by a dual frequency (2+27 or 1+27 MHz) power source. The other electrode is grounded. The computation is based on a one-dimensional coordinate space and three-dimensional ve-

locity space PIC/MC algorithm. The motion of the charged particles is simulated by the PIC method using the standard explicit "leap frog" finite difference scheme. The collisions between the charged particles are added by combining the PIC model with a MC procedure [18–20]. In the case of modeling of electronegative discharges the major disadvantage of this method is that it requires a long computational time to reach convergence. The negative charges are confined in the bulk plasma and the only the loss mechanism, i.e., ion-ion recombination, has a relatively low reaction frequency. Kawamura *et al.* point out many physical and numerical methods of speeding up the PIC calculations [31]. Some of these methods, such as longer ion time steps, different weights for electrons and ions, and improved initial density profiles, are also applied in the present simulation. A more detailed description of the PIC technique can be found in Birdsall and Langdon [17].

The charged species, which are followed in the model, are electrons, Ar^+, CF_3^+, N_2^+, F^-, and CF_3^- ions. The interactions between the particles are treated by a Monte Carlo method, which is basically a probabilistic approach. To calculate collision probabilities, it is necessary to have the corresponding collision cross-section data, which are not always available. Hence, the present model uses several techniques to define the collision probabilities even when the collision cross sections are unknown.

The electron-neutral collision probability is determined by the null collision method based on cross section data [19,20]. The Ar^+-Ar, Ar^+-N_2, N_2^+-N_2, and N_2^+-Ar collision probabilities are calculated in the same way. The other ion-neutral elastic and reactive collisions included in the model are calculated by an ion-molecule collision model for endothermic reactions [32]. The positive-negative ion recombination and electron-ion recombination probabilities are determined from a recombination rate constant [33]. The outlines of all techniques are given in our previous papers [22,23]. The electron-neutral collisions considered in this simulation, along with the corresponding threshold energies and references, are presented in Table I.

The Ar^+-Ar and N_2^+-N_2 elastic isotropic and backward scattering (to simulate charge transfer) cross sections are taken from Phelps [38]. The cross section data for nonresonant charge transfer between Ar^+ and N_2 and between N_2^+ and Ar are adopted from Spalburg and Gislason [39].

A complete overview of the ion-CF_4 reactions considered in the model (127 in total) and of the corresponding thermodynamic threshold energies, is given in Ref. [22]. Because of the importance of ion-neutral collisions for the calculation of the IEDF all data used in the model are presented in the form of cross sections in the Appendix. The positive-negative ion and electron-ion recombination reactions, the corresponding rate constants, and the references, are presented in Table II.

B. Analytical model of the IEDF in a dual-frequency reactor

The bombardment IEDF is determined by the potential difference across the sheath $V_s(x,t)$, the collision frequency (i.e., gas pressure), the sheath width s, the mass of the ions M, and the applied frequency ω_{rf}. In the literature, a number

TABLE I. Electron-neutral (Ar, CF_4, N_2) collisions taken into account in the model.

Reaction	ε_{th} (eV)	Ref.
$e + Ar \rightarrow e + Ar$		[34]
$e + Ar \rightarrow e + Ar^*$	11.5	[34]
$e + Ar \rightarrow 2e + Ar^+$	15.8	[34]
$e + N_2 \rightarrow e + N_2^*(Y)^a$		[35]
$e + N_2 \rightarrow 2e + N_2^+(Y)^b$	15.6	[35]
$e + N_2 \rightarrow 2e + N_2^+(B\ ^2\Sigma)$	18.8	[35]
$e + CF_4 \rightarrow e + CF_4$		[36]
$e + CF_4 \rightarrow e + CF_4(v1)$	0.108	[36]
$e + CF_4 \rightarrow e + CF_4(v3)$	0.168	[36]
$e + CF_4 \rightarrow e + CF_4(v4)$	0.077	[36]
$e + CF_4 \rightarrow e + CF_4^*$	7.54	[36]
$e + CF_4 \rightarrow F^- + CF_3$	6.4	[36]
$e + CF_4 \rightarrow F + CF_3^-$	5	[37]
$e + CF_4 \rightarrow e + F^- + CF_3^+$	12	[37]
$e + CF_4 \rightarrow 2e + F + CF_3^+$	16	[36]
$e + CF_4 \rightarrow e + F + CF_3$	12	[36]
$e + CF_4 \rightarrow e + 2F + CF_2$	17	[36]
$e + CF_4 \rightarrow e + 3F + CF$	18	[36]

^{a}N2$^*(Y) = N_2$ ($v = 0-8$, $A\ ^3\Sigma$, $B\ ^3\Pi$, $W\ ^3\Delta$, $B'\ ^3\Sigma$, $a'\ ^1\Sigma$, $a\ ^1\Pi$, $w\ ^1\Delta$, $C\ ^3\Pi$, $E\ ^3\Sigma$, $a''\ ^1\Sigma$, and "sum of singlets," including dissociation).
^{b}N$_2^+(Y) = N_2^+$ ($X\ ^2\Sigma$ and $A\ ^2\Pi$).

of simple analytical models have been applied for a collisionless sheath, assuming a sinusoidal sheath voltage and constant sheath width [9–11]. In HF regime the ions cross the sheath in a time corresponding to many rf cycles and they respond to the average sheath potential drop $\bar{V}_s$. If the time and space dependence of the sheath voltage is described by [11]

$$V_s(x,t) = \bar{V}_s[1 + \lambda \sin(\omega_{rf}t)]\left(\frac{x}{s}\right)^{4/3}, \qquad (2)$$

where λ is a parameter and $\lambda \leq 1$, and x is the position of the ion in the sheath, then the IEDF $f(E)$ of the ions with constant flux Γ is a saddle-shaped distribution [11]

$$f(E) = \frac{2\Gamma}{\omega_{rf}\Delta E}\left[1 - \left(\frac{2}{\Delta E}\right)^2 (E - e\bar{V}_s)^2\right]^{-1/2}, \qquad (3)$$

TABLE II. Positive-negative ion and electron-positive ion recombination reactions considered in the model and the corresponding recombination rate coefficients.

Reaction	Rate constant (m³/s)	Ref.
$F^- + Ar^+ \rightarrow F + Ar$	1.0×10^{-13}	[40]
$F^- + CF_3^+ \rightarrow F + CF_3$	1.0×10^{-13}	[40]
$CF_3^- + Ar^+ \rightarrow CF_3 + Ar$	1.0×10^{-13}	[40]
$CF_3^- + CF_3^+ \rightarrow CF_3 + CF_3$	1.0×10^{-13}	[40]
$e + CF_3^+ \rightarrow CF_3$	$3.95 \times 10^{-15}/\sqrt{T_e T_i}$	[33]
$e + N_2^+ \rightarrow 2N(^4S)$	$4.8 \times 10^{-13}\sqrt{300/T_e(K)}$	[41]

with an energy width ΔE [11]

$$\Delta E = \frac{8\lambda e\bar{V}_s}{3\omega_{rf}S}\left(\frac{2e\bar{V}_s}{M}\right)^{1/2}. \qquad (4)$$

It is clear that the result of the analytical model presented above cannot be applied for the dual frequency regime, shown in Fig. 1. To develop a simple analytical model for the dual frequency regime we make the same assumption as in a single HF reactor, except for the wave form of the sheath potential, i.e., a collisionless sheath and a constant sheath width are assumed. The applied voltage is $V = V_{HF}\sin(\omega_{HF}t) + V_{LF}\sin(\omega_{LF}t)$, where V_{HF} and V_{LF} are the amplitude, and ω_{HF} and ω_{LF} are the applied HF (27 MHz) and LF (1 or 2 MHz), respectively. In our simulation the two rf sources have the same voltage amplitude, which has a value of 700 V. The numerical simulation result of the potential across the sheath at the driven electrode in 2 LF cycles for the $(2 + 27)$ MHz case is presented in Fig. 2(a). The calculations give also the values of the mean sheath potential $\bar{V}_s$ and the average sheath width $\bar{s}$, which are used in the analytical model (see below). Figures 2(b) and 2(c) show that the sheath potential drop at the driven electrode is better described with the product of 2 harmonic functions than with the sum of them:

$$V_s(t) = \bar{V}_s[1 + \lambda_1 \sin(\omega_{HF}t)][1 + \lambda_2 \sin(\omega_{LF}t)], \qquad (5)$$

where λ_1 and λ_2 are parameters and λ_1, $\lambda_2 \lesssim 1$. The parameters λ_1 and λ_2 are determined from the plot [Fig. 2(a)] considering two time points at $\omega_{LF}t = \pi/2$ and $\omega_{LF}t = 3\pi/2$. The average sheath potential $\bar{V}_s$ is calculated in the simulation. It should be mentioned that when the primary frequency is much higher than the secondary frequency, as in the present reactor, the IEDF and energy width equations are the same for the two analytical waveforms of $V_s(t)$, presented in Figs. 2(b) and 2(c). However, the calculated λ_1 and λ_2 differ a lot, which results in a big difference in the energy width ΔE [see below Eq. (13)].

Next, we assume a spatial dependence of the sheath voltage $V_s(x,t) = V_s(t)[x(t)/s]^{4/3}$ [see Eq. (2)], providing that there are no electrons in the sheath, i.e., $\exp(eV_s/kT_e) \ll 1$ [11,21]. Therefore, the equation of motion is

$$M\frac{d^2x}{dt^2} = \frac{4}{3}\frac{e\bar{V}_s}{s}[1 + \lambda_1 \sin(\omega_{HF}t)][1 + \lambda_2 \sin(\omega_{LF}t)]\left(\frac{x}{s}\right)^{1/3}. \qquad (6)$$

To make an analytical integration of Eq. (6) we assume that the ion path $x(t)$ is close to that corresponding to the average acceleration, i.e. [11],

$$\frac{x(t)}{s} = \left[\frac{1}{3s}\left(\frac{2e\bar{V}_s}{M}\right)^{1/2}\right]^3 (t - t_0)^3, \qquad (7)$$

where t_0 is the time at which the ion enters the sheath. This approximation is valid as long as the ion transit time τ_{ion} is longer than or equal to the rf period. In our case this applies
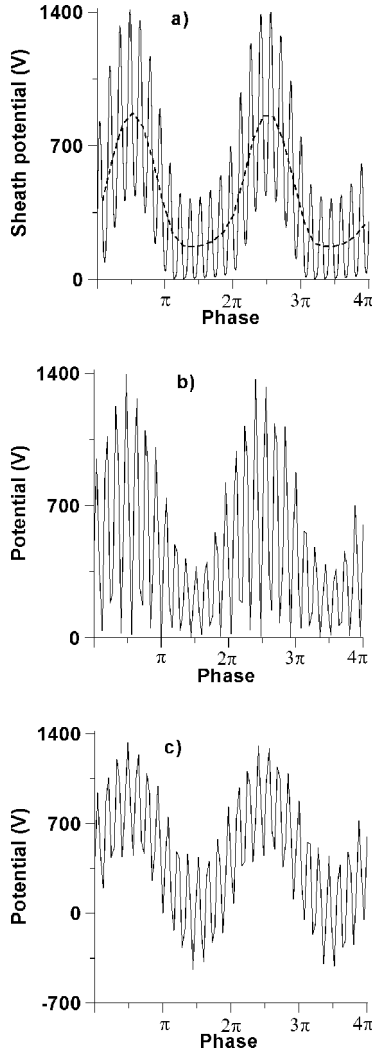
FIG. 2. Sheath potential at the driven electrode in the dual frequency (27+2) MHz reactor in 2 LF cycles: (a) numerical result, (b) analytical function $V_s(t) = \bar{V}_s[1 + \lambda_1 \sin(\omega_{HF}t)][1 + \lambda_2 \sin(\omega_{LF}t)]$, and (c) analytical function $V_s(t) = \bar{V}_s[1 + \lambda_1 \sin(\omega_{HF}t) + \lambda_2 \sin(\omega_{LF}t)]$. The applied voltage amplitude V_{rf} is 700 V and the calculated $\bar{V}_s$ is 445 V. The dashed line in (a) shows the averaged HF sheath potential as a function of the LF.

to the LF period τ_{LF} because $\tau_{LF} \gg \tau_{HF}$ and hence, when $\tau_{ion}/\tau_{LF} \gtrsim 1$, this means that $\tau_{ion}/\tau_{HF} \gtrsim 1$ is also true. This implies

$$\omega_{LF}(t - t_0) = 2\pi \tau_{ion}/\tau_{LF} \gg 1. \qquad (8)$$

In the simulation in the (2+27) MHz case τ_{ion}/τ_{LF} is calculated to be 0.9, 1.2, and 0.7 for Ar^+, CF_3^+, and N_2^+ ions, respectively. Therefore, the assumption presented above can be made. In the (1+27) MHz case these values are 0.5, 0.6, and 0.4, respectively, which means that the ion path cannot be assumed close to the average, in particular for N_2^+. As will be seen in Sec. III in this case the deviation of the analytical from the numerical results is larger.

Substituting Eq. (7) in the equation of motion (6) leads to

$$\frac{d^2x}{dt^2} = \frac{2}{9s^2}\left(\frac{2e\bar{V}_s}{M}\right)^{3/2}[1 + \lambda_1 \sin(\omega_{HF}t)]$$

$$\times [1 + \lambda_2 \sin(\omega_{LF}t)](t - t_0). \qquad (9)$$

Taking into account that $\omega_{HF} \gg \omega_{LF}$ and Eq. (8) is true, the time integration of Eq. (9) yields the velocity

$$\frac{dx}{dt} = \frac{2}{9s^2\omega_{LF}^2}\left(\frac{2e\bar{V}_s}{M}\right)^{3/2}$$

$$\times \left[\frac{1}{2}\omega_{LF}^2(t - t_0)^2 - \lambda_2\omega_{LF}(t - t_0)\cos(\omega_{LF}t)\right]. \qquad (10)$$

The time of arrival at the electrode $t_1 [x(t_1) = s]$ is obtained from the average ion path (7):

$$(t_1 - t_0) = 3s\left(\frac{M}{2e\bar{V}_s}\right)^{1/2}. \qquad (11)$$

Thus, the energy of the ions arriving at the electrode is

$$E = e\bar{V}_s\left[1 - \frac{2\lambda_2}{3s\omega_{LF}}\left(\frac{2e\bar{V}_s}{M}\right)^{1/2}\cos(\omega_{LF}t_1)\right]^2$$

$$\approx e\bar{V}_s\left[1 - \frac{4\lambda_2}{3s\omega_{LF}}\left(\frac{2e\bar{V}_s}{M}\right)^{1/2}\cos(\omega_{LF}t_1)\right] \qquad (12)$$

and it is spread over the energy width ΔE, centered at $e\bar{V}_s$,

$$\Delta E = \frac{8\lambda_2}{3s\omega_{LF}}\left(\frac{2e\bar{V}_s}{M}\right)^{1/2}. \qquad (13)$$

Finally, we obtain the IEDF $f(E)$ of the ions with constant flux $\Gamma = dN/dt_1$

$$f(E) = \frac{dN}{dE} = \frac{dN}{dt_1}\left(\frac{dE}{dt_1}\right)^{-1}$$

$$= \frac{2\Gamma}{\omega_{LF}\Delta E}\left[1 - \left(\frac{2}{\Delta E}\right)^2(E - e\bar{V}_s)^2\right]^{-1/2}. \qquad (14)$$

Equation (13) shows that the energy width in the dual frequency regime depends only on the applied LF. This result is reasonable because the ion transit time is much longer than the HF period. Indeed, the ratio τ_{ion}/τ_{HF} is calculated to be 12, 16, and 10 for Ar^+, CF_3^+, and N_2^+ ions, respectively. Consequently, the ions respond to the average HF potential, which is a function of the LF [see the dashed line in Fig. 2(a)].

III. RESULTS AND DISCUSSION

All the calculations are performed for an $Ar/CF_4/N_2$ mixture at a ratio of 0.8/0.1/0.1. The gas temperature is set to 300 K. The simulation grid is uniform and it consists of 100 cells. The electron time step is 3.7×10^{-11} s. To speed up the
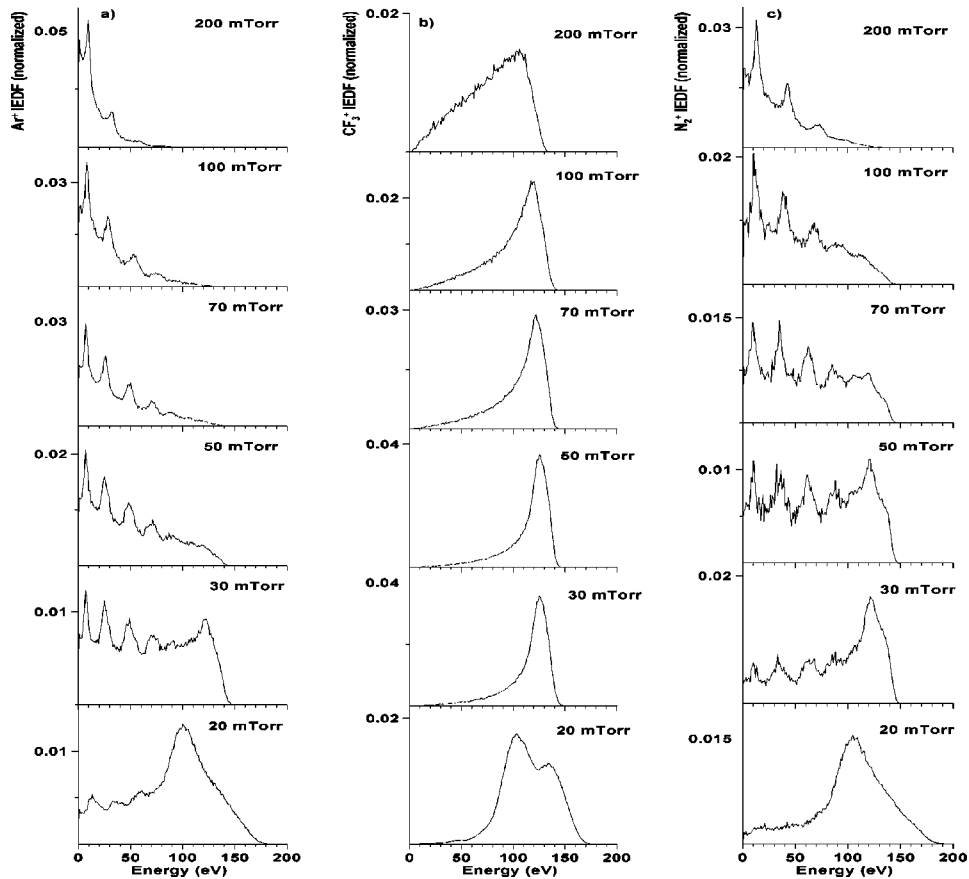
FIG. 3. Ar$^+$ (a), CF$_3^+$ (b), and N$_2^+$ (c) IEDFs at the powered electrode, averaged over one HF (13.56 MHz) cycle in the conventional cc rf reactor at pressure 20, 30, 50, 70, 100, and 200 mTorr. The applied voltage amplitude is 300 V.

calculation, the ion time step is set to be 25 times longer than the electron time step. The choice of the grid spacing and the time steps is defined by the accuracy criteria for PIC/MC codes with explicit mover [31].

A. Effect of pressure

Figure 3 presents the simulation results of the Ar$^+$ (a), CF$_3^+$ (b), and N$_2^+$ (c) IEDFs at the powered electrode, averaged over one HF (13.56 MHz) cycle in the conventional cc rf reactor at pressures of 20, 30, 50, 70, 100, and 200 mTorr. The applied voltage amplitude is 300 V. At the applied HF the ions traverse the sheath in a time corresponding to many rf cycles and hence the IEDFs reflect the time averaged sheath potential. Therefore, following the analytical models it is expected that in a collisionless sheath the IEDFs will be narrow with one or two peaks and centered at $e\bar{V}_s$ [see Eqs. (3) and (4), and Refs. [9–11]]. The collisionless approximation in the present simulation can be made only at a very low pressure. It is clearly seen in Fig. 3 that at a pressure of 20 mTorr the collisional effects in the sheath are not very prominent, especially for the CF$_3^+$ IEDF. In all presented simulations CF$_3^+$-neutral-elastic collisions are considered; the charge transfer reaction CF$_3^+$-CF$_3$ is not taken into account since the density of the CF$_3$ radicals is much lower in comparison with the CF$_4$ density, with a value in the order of

10^{18} m^{-3} in a pure CF$_4$ discharge [42,43]. Although the ions lose kinetic energy in the reactive collisions (see the Appendix), their energy distribution is influenced by the reactive collisions only at high pressure (200 mTorr). Consequently, the CF$_3^+$ IEDF shows the influence of the elastic collisions. With increasing pressure the two peaks coincide and move towards lower energy (from 125 eV at 20 mTorr to 110 eV at 200 mTorr) [Fig. 3(b)]. The calculated averaged sheath potential is 125 V.

The simulations take into account both elastic and charge transfer (resonant and nonresonant) collisions between Ar$^+$ or N$_2^+$ and Ar or N$_2$. Secondary peaks are observed in the Ar$^+$ and N$_2^+$ IEDFs, and they are due to the charge exchange collisions [see Figs. 3(a) and 3(c) with the CF$_3^+$ IEDF in Fig. 3(b)]. Obviously, for Ar$^+$ and N$_2^+$ ions the charge exchange collision frequency is much higher than the elastic collision frequency [11]. Hence, the Ar$^+$ and N$_2^+$ IEDFs mainly present the contribution of the charge transfer collisions (see the ion-neutral collision cross sections presented in the Appendix). Figures 3(a) and 3(c) show that increasing the pressure leads to increasing the intensity of the secondary peaks. Moreover, the distance between them rises and the number of the peaks decreases. At the same time the primary peaks become less intense and at some pressure, they even disappear. This is caused by the increasing collision frequency in the sheath, which in turn is due to the shorter mean free path.
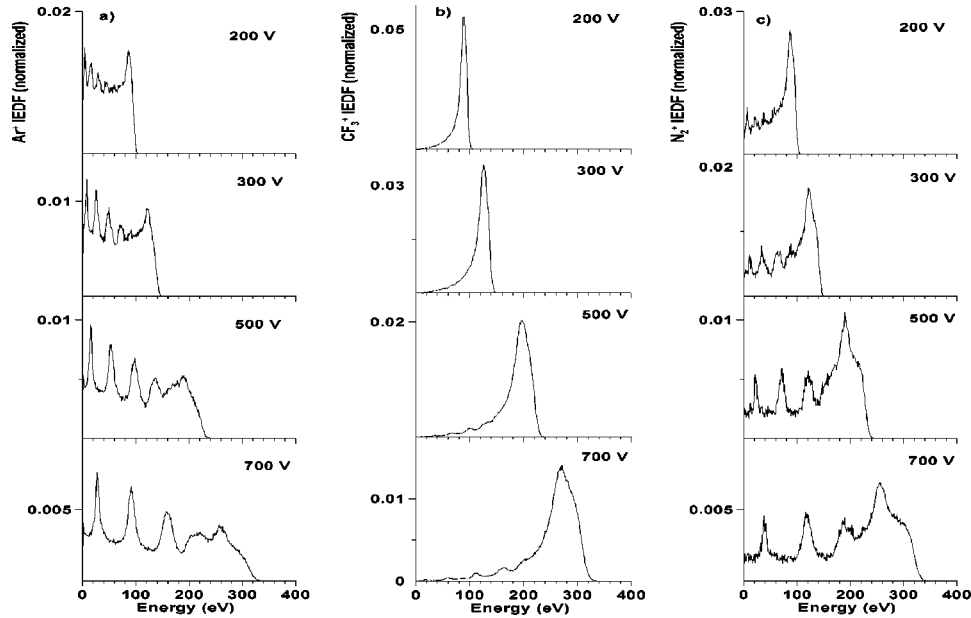
FIG. 4. Ar^+ (a), CF_3^+ (b), and N_2^+ (c) IEDFs at the powered electrode, averaged over one HF (13.56 MHz) cycle in the conventional cc rf reactor at pressure 30 mTorr and applied voltage amplitude 200, 300, 500, and 700 V.

As a result more and more ions take part in at least one collision on their way towards the electrode and their energy is shifted to lower values. These observations are in consistency with a number of works investigating the influence of pressure on the IEDF (mainly of Ar^+ ions) considering both elastic and charge transfer collisions (e.g., Refs. [2–6], [8], [10–16]).

B. Effect of the applied voltage amplitude

Figure 4 presents the simulation results of the Ar^+ (a), CF_3^+ (b), and N_2^+ (c) IEDFs at the powered electrode, averaged over one HF (13.56 MHz) cycle in the conventional cc rf reactor at a pressure of 30 mTorr and applied voltage amplitude V_{rf} of 200, 300, 500, and 700 V. It can be seen that the amplitude of the applied voltage has a significant effect on the width of the IEDF and the magnitude of the peaks. Indeed, the average sheath potential increases with increasing V_{rf}, which results in broader IEDFs and in a shift of the primary peaks to higher energies. The influence of the charge transfer and elastic collisions can be observed in the Ar^+ and N_2^+ IEDFs, and in the CF_3^+ IEDF, respectively (see Fig. 4). The number of secondary peaks and their intensity decreases, and the gap between them increases with increasing applied voltage amplitude. This is related to a drop in the sheath width and a rise in the plasma density, which in turn results in increasing the ion plasma frequency [2]. These simulation results are in consistency with a number of experimental and theoretical works investigating the influence of the applied voltage on the IEDF (e.g., Refs. [2–8], [15]). The present detailed investigation of the three different ions (Ar^+, CF_3^+, and N_2^+) demonstrates not only the influence of the pressure and applied voltage on the IEDF but also the influence of the different types of ion-neutral collisions.

C. Effect of the applied frequency regime

Figure 5 (solid lines) presents the simulation results of the Ar^+ (a), CF_3^+ (b), and N_2^+ (c) IEDFs at the powered electrode, averaged over two LF (2 MHz) cycles and over one LF (1 MHz) cycle in the dual frequency reactor at a pressure of 30 mTorr and the applied voltage amplitude of 700 V. In the $(2+27)$ MHz case the IEDFs are averaged over two LF cycles since one LF cycle does not contain an integer number of HF cycles. The analytical calculation results based on Eqs. (13) and (14) are also given in Fig. 5, with dashed lines. A comparison with the IEDFs at the same operating conditions in the single frequency reactor (Fig. 4 at applied voltage amplitude 700 V, i.e., the lowest plots) shows that the dual frequency regime provides a significantly wider ion bombardment energy range, which is one of the main advantages of the dual frequency reactors used in plasma etching [23–30]. For example, in the HF regime the maximum Ar^+ ion energy is calculated to be only 350 eV, while in the $(2+27$ MHz) regime it is calculated to be 700 eV. The increase of the maximum ion energy with the addition of low frequency to the plasma system is also predicted by the numerical simulation, presented by Myers *et al.* [16]. In the presence of LF the ion transit time τ_{ion} is less than the LF period τ_{LF}, i.e., the ions cross the sheath in a fraction of the LF cycle and they reach the electrode with an energy equal to the instantaneous sheath potential drop (see the calculated τ_{ion}/τ_{LF} for the three investigated ions, presented in Sec. II) [10,11].

The two outstanding peaks in the profiles, presented in Fig. 5, correspond to the averaged minimum and maximum sheath potentials [cf. Fig. 2(a), dashed line]. The peak intensity at the lower energy is higher because the sheath potential has an average minimum value for a longer time than an average maximum value [4,10].
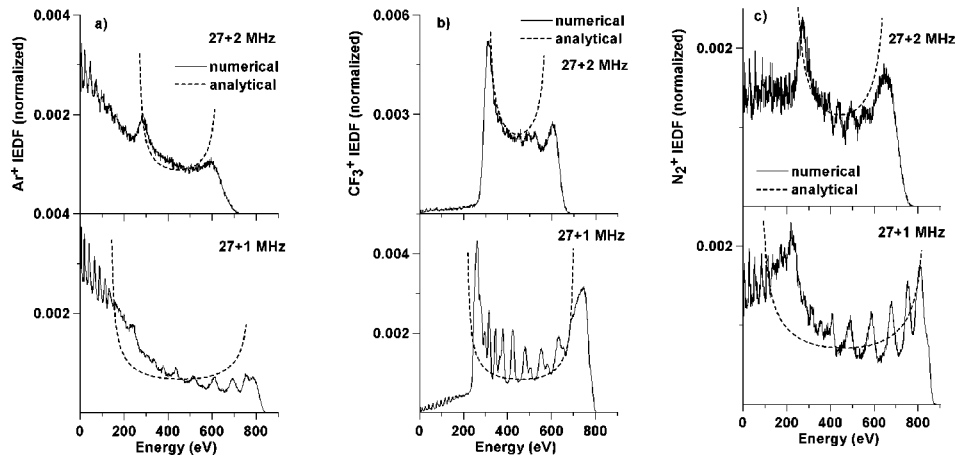
FIG. 5. Ar^+ (a), CF_3^+ (b), and N_2^+ (c) IEDFs at the powered electrode, averaged over 2 LF (2 MHz) cycles and over 1 LF (1 MHz) cycle in the dual frequency reactor at pressure 30 mTorr and applied voltage amplitude 700 V (solid lines). The analytical calculation results are given with the dashed lines.

The influence of the collisions is the same as discussed in the conventional cc rf (13.56 MHz) reactor (see above). However, at the (1+27) MHz scheme secondary peaks are observed in the CF_3^+ IEDF although no charge transfer collisions are included. The reason is probably the frequency of 1 MHz (2 times lower compared to 2 MHz) in which the ions respond to the instantaneous HF potential as a function of the LF.

The results of the simple analytical model developed in Sec. II are in good agreement with the simulation results in the (2+27) MHz regime (Fig. 5, upper part) and to a lesser extent with the simulation results in the (1+27) MHz regime (Fig. 5, lower part). Although the analytical model does not consider collisions we suggest that this consistency is a result of the good sheath potential wave form approximation. The energy width is calculated from Eq. (13) with the values of $\bar{V}_s$ and average sheath width s, obtained from the simulation. The parameter λ_2 is determined from the plot of the sheath potential (see Sec. II). In the (2+27) MHz regime the calculated $\bar{V}_s$, s, and λ_2 are equal to 445 V, 6.8×10^{-3} m, and 0.55, respectively. The plots are fitted in such a way that the analytical value of $f(E)$ at $e\bar{V}_s$ is equal to that calculated in the simulation. Hence, we should not focus on the absolute values of the analytical curves, but only on the energy width and the position of the two peaks. As can be seen in the (1+27) MHz scheme $2\pi\tau_{ion}/\tau_{LF}$ is larger than but close to 1 (see Sec. II) and consequently, Eq. (8) is not valid, which leads to a discrepancy between the numerical and analytical calculations of the energy width and the position of the peaks (see Fig. 5, lower part). In this regime the calculated $\bar{V}_s$, s, and λ_2 are equal to 459 V, 7.4×10^{-3} m, and 0.52, respectively. The present results show that the developed analytical model can be used to predict the positions of the primary peaks in the dual frequency regime if condition (8) is satisfied.

Finally, the IEDFs at different times of the HF cycle in the single frequency regime and at different times of the LF cycle in the dual frequency regime are presented in Figs. 6 and 7. The Ar^+ IEDF in single and dual frequency reactors is

shown in Figs. 6(a) and 6(b), respectively. The CF_3^+ IEDF in single and dual frequency reactors is shown in Figs. 7(a) and 7(b), respectively. The profile of the N_2^+ IEDF is similar to the Ar^+ IEDF, and is therefore not shown. Obviously, in the HF regime the ions respond only to the average sheath drop and their energy distribution is peaked close to $\overline{eV_s}$ ($\bar{V}_s$ is
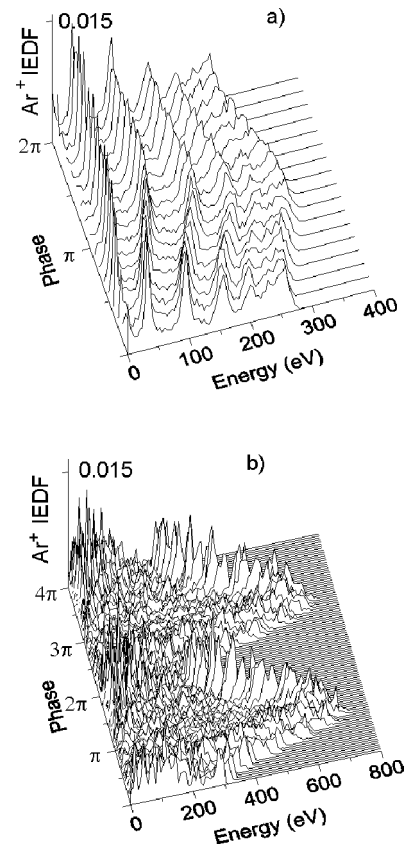
FIG. 6. Ar^+ IEDF at different phases in one HF cycle in the single (13.56 MHz) frequency reactor (a) and at different phases in 2 LF cycles in the dual (27+2 MHz) frequency reactor (b) at pressure 30 mTorr and applied voltage amplitude 700 V.
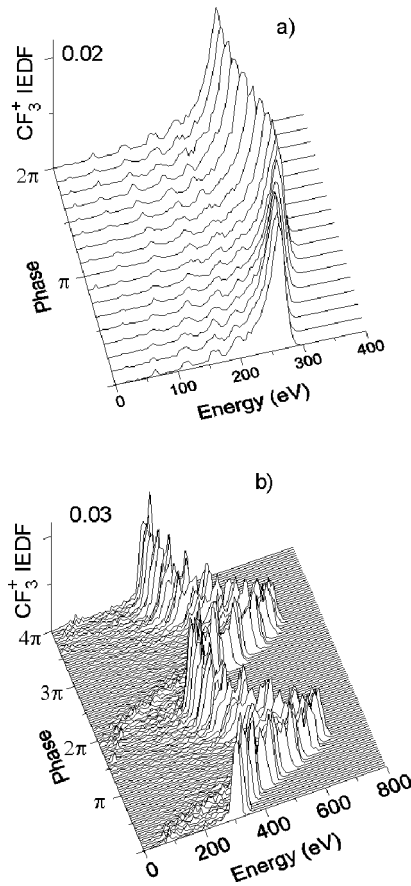
FIG. 7. CF_3^+ IEDF at different phases in one HF cycle in the single (13.56 MHz) frequency reactor (a) and at different phases in 2 LF cycles in the dual (27+2 MHz) frequency reactor (b) at pressure 30 mTorr and applied voltage amplitude 700 V.

FIG. 8. $Ar^+ + Ar$ charge transfer (1) and $Ar^+ + Ar$ elastic isotropic scattering (2) cross sections as a function of the laboratory ion energy in eV, and $Ar^+ + N_2$ charge transfer (3) cross section as a function of the relative energy in eV.

calculated to be 285 V) [Figs. 6(a) and 7(a)]. In the dual frequency regime [Figs. 6(b) and 7(b)] a great modulation of the IEDF is observed during the LF cycle. The ion transit time is close to the LF period (see the calculated τ_{ion}/τ_{LF} given in Sec. II) and the ions respond to the instantaneous sheath potential. The time dependence in the rf cycle presented in Figs. 6 and 7 is a demonstration of the main observation summarized in the Introduction.

IV. SUMMARY

Ar^+, CF_3^+, and N_2^+ IEDFs are numerically investigated in $Ar/CF_4/N_2$ discharges in cc single and dual frequency reactors by a one-dimensional PIC/MC model. The model considers electron-neutral collisions, various kinds of collisions of ions (Ar^+, CF_3^+, N_2^+, F^-, and CF_3^-) with neutral, positive-negative ion, and electron-ion recombination. The influence of pressure, applied voltage amplitude, and applied frequency regime on the IEDFs is discussed.

The simulations are carried out over a wide range of pressure and applied voltage amplitude covered in the conventional cc plasma etching reactors. The results show that the IEDFs shift toward low energies with increasing pressure or decreasing applied voltage amplitude. The influence of the

different types of ion-neutral collisions is presented for the three investigated ions.

The dependence on the frequency regime is investigated by simulations in single (13.56 MHz) and dual frequency (2+27 MHz or 1+27 MHz) cc reactors. It is observed that the dual frequency regime provides a significantly wider ion bombardment energy range in comparison with the single frequency regime. An analytical model for the IEDF in a collisionless sheath for the dual frequency reactor is developed and a comparison with the numerical calculation is discussed. The analytical model can be used to predict the position of the primary peaks.

Finally, the time dependences of the IEDFs in an rf cycle in single (HF) and dual (LF-HF) frequency reactors are presented. It is shown that in the HF regime the IEDF slightly depends on the phase of the rf cycle, whereas in the LF-HF regime the IEDF is greatly modulated during the LF cycle.

APPENDIX

Because of the importance of ion-molecule collisions for the calculation of the IEDFs, we present the data about ion-neutral collisions used in the model in some more detail. Figure 8 presents the Ar^+-Ar elastic isotropic scattering and scattering in the backward direction (to simulate charge
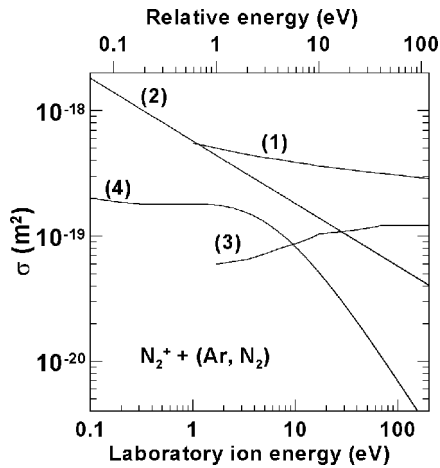
FIG. 9. $N_2^+ + N_2$ charge transfer (1), $N_2^+ + N_2$ elastic isotropic scattering (2), and $N_2^+ + Ar$ elastic isotropic scattering (4) cross sections as a function of the laboratory ion energy in eV, and $N_2^+ + Ar$ charge transfer (3) cross section as a function of the relative energy in eV.

transfer) cross sections as a function of the laboratory ion energy in eV, and Ar^+-N_2 charge transfer cross sections as a function of the relative energy ε in eV [38,39]. The Ar^+-CF_4 and Ar^+-N_2 elastic collisions are not considered in the present simulations since the density of CF_4 and N_2 is low compared to that of Ar and consequently, the probabilities for collisions are small. Similarly, N_2^+-CF_4 and $CF_x^{+/-}$ ions-N_2 collisions are neglected in the model.

Figure 9 shows the N_2^+-N_2 elastic isotropic scattering and charge transfer, and N_2^+-Ar elastic isotropic scattering cross sections as a function of the laboratory ion energy in eV, and N_2^+-Ar charge transfer cross section as a function of the relative energy in eV [38,39]. The cross section for N_2^+-N_2 elastic isotropic scattering Q_i is approximated up to 50 eV to the Langevin cross section for polarization scattering and for energies higher than 50 eV to ($Q_m - 2Q_{CT}$) as was done for the Ar^+-Ar elastic isotropic cross section in Ref. [38]. Q_m and Q_{CT} are the momentum and charge transfer cross sections, respectively. The data for N_2^+-Ar elastic isotropic scattering cross section are estimated from the data available for the Ar^+-Ar collisions taking into account that $Q_i \sim 1/\sqrt{\mu}$, where μ is the reduced mass.

In the model, the $CF_x^{+/-}$-ion–neutral (CF_4 and Ar) collisions are treated by means of the ion-molecule collision model for endothermic reactions, described in Refs. [22], [32], and [45]. The CF_3^+-CF_4 and Ar elastic and reactive collision cross sections, the F^--CF_4 reactive collision cross sections, and the CF_3^--CF_4 reactive collision cross sections are presented in Figs. 10(a), 10(b), and 10(c), respectively. The cross sections for the reactive collisions σ_r are calculated from the probabilities, given by Eq. (5) in Ref. [22] in case that the relative energy of the reactants is greater than the least threshold energy ΔE, and the randomly sampled dimensionless impact parameter $\beta \lesssim 1$. Let us remind the reader that the "elastic reactive" collision (see Ref. [22]) is treated as elastic with isotropic scattering, i.e., the velocity of the ion after the collisions is calculated by Eq. (63a) in Ref.
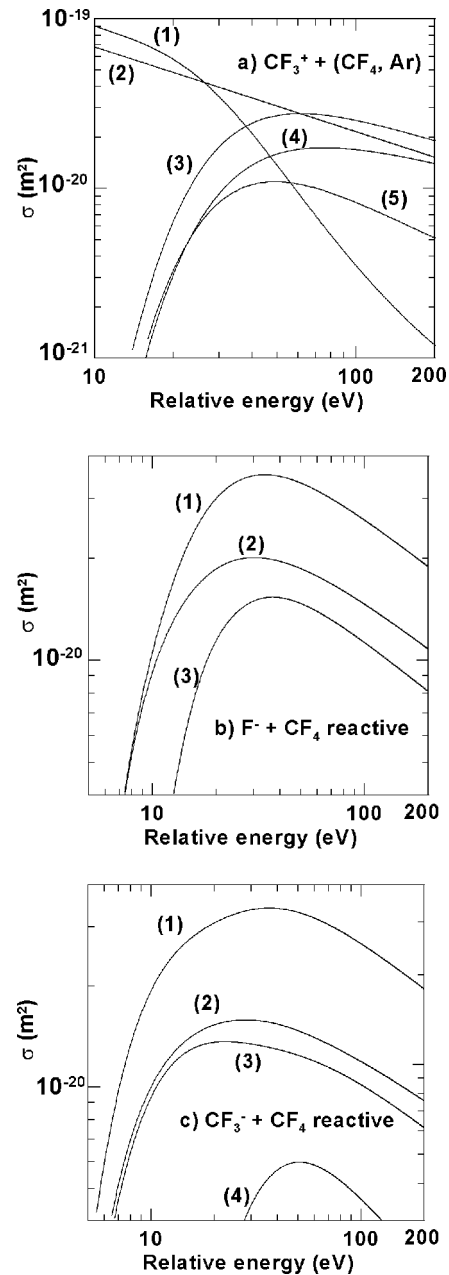
FIG. 10. (a) $CF_3^+ + (CF_4, Ar)$ cross sections. $CF_3^+ + CF_4$ (1) and $CF_3^+ + Ar$ (2) elastic isotropic scattering; sum of all reactive $CF_3^+ + CF_4$ collisions (3); sum of reactive $CF_3^+ + CF_4$ with a loss of CF_3^+ ion (4); and sum of reactive $CF_3^+ + CF_4$ collisions after which the CF_3^+ ion is one of the products (5). (b) $F^- + CF_4$ cross sections; Sum of all reactive $F^- + CF_4$ collisions (1); sum of electron detachment (2); and sum of reactive $F^- + CF_4$ collisions after which the F^- ion is one of the products (3). (c) $CF_3^- + CF_4$ cross sections. Sum of all reactive $CF_3^- + CF_4$ collisions (1); sum of electron detachment (2); sum of reactive $CF_3^- + CF_4$ collisions after which the F^- ion is one of the products (3); and sum of reactive $CF_3^- + CF_4$ collisions after which the CF_3^- ion is one of the products (4).

[44]. Elastic isotropic scattering is also assumed if the relative energy of the reactants is less than the least threshold energy and $\beta \lesssim 1$. The cross sections for $CF_x^{+/-}$ ions $+ CF_4$ elastic isotropic scattering collisions are calculated from the

probability, given by Eq. (6) in Ref. [22] in the case where $\beta \leq 1$. Only the CF_3^+-CF_4 and Ar elastic isotropic cross sections are shown [Fig. 10(a) curves (1) and (2)] because the F^--CF_4 and Ar and the CF_3^--CF_4 and Ar elastic cross sections have similar values. If $\beta > 1$ the collision is treated as elastic with anisotropic scattering [22,32]. The deflection angle is a function of β and the post collision velocities are calculated as is described in Ref. [44]. Since $\beta = \beta_\infty \sqrt{R}$, where β_∞ is set to 3 and R is a random number between 0 and 1 (see Ref. [22]) the contribution of the anisotropic scattering prevails that of the isotropic scattering. The cutoff parameter β_∞ is the value of β, for which the deflection angle is negligibly small [22,45].

In the case of reactive collisions the velocities of the products are calculated based on the energy and momentum conservation, which is illustrated by the following example [45]. The reaction with threshold energy ΔE

$$CF_3^+ + CF_4 \rightarrow CF_2^+ + CF_3 + 2F$$

is divided into three stages. A complex $C_2F_7^+$ ion is formed and then the excited ion and neutral [45]

$$CF_3^+ + CF_4 \rightarrow [C_2F_7^+] \rightarrow (CF_3^+)^* + (CF_4)^*.$$
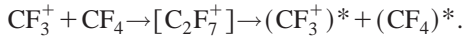
If the mass and velocity before collision of the ion and neutral are M_i, $\vec{V}_i$ and M_n, $\vec{V}_n$, respectively, the relative velocity is $g = |\vec{V}_i - \vec{V}_n|$, and the reduced mass is μ, the energy and momentum conservation are

$$\frac{1}{2}\mu g^2 = \frac{1}{2}\mu g_1^2 + \Delta E, \tag{A1}$$

$$M_i \vec{V}_i + M_n \vec{V}_n = M_i \vec{V}_{1i} + M_n \vec{V}_{1n}, \tag{A2}$$

where $g_1 = |\vec{V}_{1i} - \vec{V}_{1n}|$, $\vec{V}_{1i}$ and $\vec{V}_{1n}$ are the relative velocity, and the velocities of the excited molecules. Isotropic scattering is assumed, i.e., $\vec{V}_{1i} - \vec{V}_{1n} = g_1 \vec{R}$, where $\vec{R}$ is the unit vector with random direction [45].

In the next step, dissociation of the excited molecules follows

$$(CF_3^+)^* \rightarrow CF_2^+ + F,$$

$$(CF_4)^* \rightarrow CF_3 + F.$$
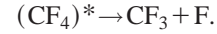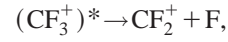
Assuming that all internal energy of the excited molecules is used for dissociation, and applying again the energy and momentum conservation, the velocities of CF_2^+ and F are equal to that of the excited ion $\vec{V}_{1i}$, and the velocities of CF_3 and F are equal to that of the excited neutral $\vec{V}_{1n}$ [45].

Since only CF_3^+, F^-, and CF_3^- ions (i.e., not the other positive CF_x ions and radicals) are followed in the model we do not present the cross section of every reaction, given in Ref. [22]. Figure 10(a) shows the sum of all reactive CF_3^+ $+ CF_4$ collisions (3), the sum of reactive collisions in case of dissociation of the initial ion, i.e., loss of the ion (4), and the sum of the reactive collisions after which one of the products is the initial ion (5). In the last case (5) there is no production of the ion, only its energy is reduced more or less significantly (see above). However, this kind of collision cannot be considered as symmetric charge transfer since the postcollision velocity of the ion is not close to the thermal velocity of the neutrals.

Similarly, Fig. 10(b) presents cross sections of the sum of all reactive $F^- + CF_4$ collisions (1), the sum of electron detachment collisions (2), and the sum of reactive collisions after which F^- is one of the products (3). Finally, Fig. 10(c) shows cross sections of the sum of all reactive $CF_3^- + CF_4$ collisions (1), the sum of electron detachment collisions (2), the sum of reactive collisions after which F^- or CF_3^- is one of the products (3) or (4), respectively.

The presented theoretical cross section of the sum of all reactive CF_3^+-CF_4 collisions is about four times less in the range of relative energy 20–200 eV and the theoretical cross section of the electron detachment F^--CF_4 is one order of magnitude lower in the range of relative energy 10–200 eV than the values experimentally measured by Peko *et al.* [46]. In a future work we will investigate the influence of the two cross section sets on the results.

[1] W. M. Greene, M. A. Hartney, W. G. Oldham, and D. W. Hess, J. Appl. Phys. **63**, 1367 (1988).

[2] C. Wild and P. Koidl, Appl. Phys. Lett. **54**, 505 (1989); J. Appl. Phys. **69**, 2909 (1991).

[3] J. Liu, G. L. Huppert, and H. H. Sawin, J. Appl. Phys. **68**, 3916 (1990).

[4] A. Manenschijn, G. C. A. M. Janssen, E. van der Drift, and S. Radelaar, J. Appl. Phys. **69**, 1253 (1991).

[5] J. K. Olthoff, R. J. Van Brunt, and S. B. Radovanov, J. Appl. Phys. **72**, 4566 (1992); J. K. Olthoff, R. J. Van Brunt, S. B. Radovanov, J. A. Rees, and R. Surowiec, *ibid.* **75**, 115 (1994).

[6] R. J. M. M. Snijkers, M. J. M. van Sambeek, G. M. W. Kroesen, and F. J. de Hoog, Appl. Phys. Lett. **63**, 308 (1993).

[7] D. Barton, D. J. Heason, R. D. Short, and J. W. Bradley, Meas. Sci. Technol. **11**, 1726 (2000).

[8] F. Becker, I. W. Rangelow, K. Maßeli, and R. Kassing, Surf. Coat. Technol. **74–75**, 485 (1995).

[9] P. Benoit-Cattin and L. C. Bernard, J. Appl. Phys. **39**, 5723 (1968).

[10] E. Kawamura, V. Vahedi, M. A. Lieberman, and C. K. Birdsall, Plasma Sources Sci. Technol. **8**, R45 (1999).

[11] W. J. Goedheer, Plasma Sources Sci. Technol. **9**, 507 (2000).

[12] M. J. Kushner, J. Appl. Phys. **58**, 4024 (1985).

[13] A. Metze, D. W. Ernie, and H. Oskam, J. Appl. Phys. **60**, 3081 (1986).

[14] D. Vender and R. W. Boswell, IEEE Trans. Plasma Sci. **18**, 725 (1990).

[15] M. Surendra and D. B. Graves, IEEE Trans. Plasma Sci. **19**,

144 (1991).

[16] F. R. Myers, M. Ramaswami, and T. S. Cale, J. Electrochem. Soc. **141**, 1313 (1994).

[17] C. K. Birdsall and A. B. Langdon, *Plasma Physics via Computer Simulation* (McGraw-Hill, New York, 1985).

[18] C. K. Birdsall, IEEE Trans. Plasma Sci. **19**, 65 (1991).

[19] V. Vahedi and M. Surendra, Comput. Phys. Commun. **87**, 179 (1995).

[20] A. Okhrimovskyy, A. Bogaerts, and R. Gijbels, Phys. Rev. E **65**, 037402 (2002).

[21] M. A. Lieberman and A. J. Lichtenberg, *Principles of Plasma Discharges and Materials Processing* (Wiley, New York, 1994).

[22] V. Georgieva, A. Bogaerts, and R. Gijbels, J. Appl. Phys. **93**, 2369 (2003).

[23] V. Georgieva, A. Bogaerts, and R. Gijbels, J. Appl. Phys. **94**, 3748 (2003).

[24] H. H. Goto, H.-D. Löwe, and T. Ohmi, J. Vac. Sci. Technol. A **10**, 3048 (1992); H. H. Goto, H.-D. Löwe, and T. Ohmi, IEEE Trans. Semicond. Manuf. **6**, 58 (1993).

[25] V. Vahedi and G. DiPeso, J. Comput. Phys. **131**, 149 (1997).

[26] H. C. Kim and V. I. Manousiouthakis, J. Vac. Sci. Technol. A **16**, 2162 (1998).

[27] W. Tsai, G. Mueller, R. Lindquist, B. Frazier, and V. Vahedi, J. Vac. Sci. Technol. B **14**, 3276 (1996).

[28] T. Kitajima, Y. Takeo, and T. Makabe, J. Vac. Sci. Technol. A **17**, 2510 (1999); T. Kitajima, Y. Takeo, Z. Lj. Petrović, and T. Makabe, Appl. Phys. Lett. **77**, 489 (2000).

[29] S. Rauf and M. J. Kushner, IEEE Trans. Plasma Sci. **27**, 1329 (1999).

[30] K. Maeshige, G. Washio, T. Yagisawa, and T. Makabe, J. Appl. Phys. **91**, 9494 (2002).

[31] E. Kawamura, C. K. Birdsall, and V. Vahedi, Plasma Sources Sci. Technol. **9**, 413 (2000).

[32] K. Denpoh and K. Nanbu, J. Vac. Sci. Technol. A **16**, 1201 (1998).

[33] K. Nanbu and K. Denpoh, J. Phys. Soc. Jpn. **67**, 1288 (1998); K. Denpoh and K. Nanbu, Jpn. J. Appl. Phys., Part 1 **39**, 2804 (2000).

[34] A. V. Phelps and Z. Lj. Petrovic, Plasma Sources Sci. Technol. **8**, R21 (1999).

[35] A. V. Phelps and L. C. Pitchford, Phys. Rev. A **31**, 2932 (1985); A. V. Phelps *et al.*, URL ftp://jila.colorado.edu/collison_data/

[36] M. Kurihara, Z. Lj. Petrovic, and T. Makabe, J. Phys. D **33**, 2146 (2000).

[37] R. A. Bonham, Jpn. J. Appl. Phys., Part 1 **33**, 4157 (1994).

[38] A. V. Phelps, J. Phys. Chem. Ref. Data **20**, 557 (1991); A. V. Phelps, J. Appl. Phys. **76**, 747 (1994); URL ftp://jila.colorado.edu/collision_data/

[39] M. R. Spalburg and E. A. Gislason, Chem. Phys. **94**, 339 (1985).

[40] S. Rauf and M. J. Kushner, J. Appl. Phys. **82**, 2805 (1997).

[41] J. Henriques, E. Tatarova, V. Guerra, and C. M. Ferreira, J. Appl. Phys. **91**, 5622 (2002).

[42] N. V. Mantzaris, A. Boudouvis, and E. Gogolides, J. Appl. Phys. **77**, 6169 (1995); E. Gogolides, M. Stathakopoulos, and A. Boudouvis, J. Phys. D **27**, 1878 (1994).

[43] J. P. Booth, G. Cunge, P. Chabert, and N. Sadeghi, J. Appl. Phys. **85**, 3097 (1999).

[44] K. Nanbu, IEEE Trans. Plasma Sci. **28**, 971 (2000).

[45] K. Denpoh, Ph.D. thesis, Tohoku University, Sendai, Japan (in Japanese).

[46] B. L. Peko, I. V. Dyakov, R. L. Champion, M. V. V. S. Rao, and J. K. Olthoff, Phys. Rev. E **60**, 7449 (1999).